Accepted Manuscript

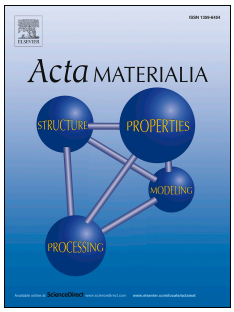

Effect of hydrogen on nanomechanical properties in Fe—22Mn-0.6C TWIP steel revealed by in-situ electrochemical nanoindentation

Dong Wang, Xu Lu, Yun Deng, Xiaofei Guo, Afrooz Barnoush

PII: S1359-6454(18)31006-1

DOI: https://doi.org/10.1016/j.actamat.2018.12.055

Reference: AM 15063

To appear in: *Acta Materialia*

Received Date: 19 October 2018

Revised Date: 27 December 2018

Accepted Date: 30 December 2018

Please cite this article as: D. Wang, X. Lu, Y. Deng, X. Guo, A. Barnoush, Effect of hydrogen on nanomechanical properties in Fe—22Mn-0.6C TWIP steel revealed by in-situ electrochemical nanoindentation, *Acta Materialia*, https://doi.org/10.1016/j.actamat.2018.12.055.

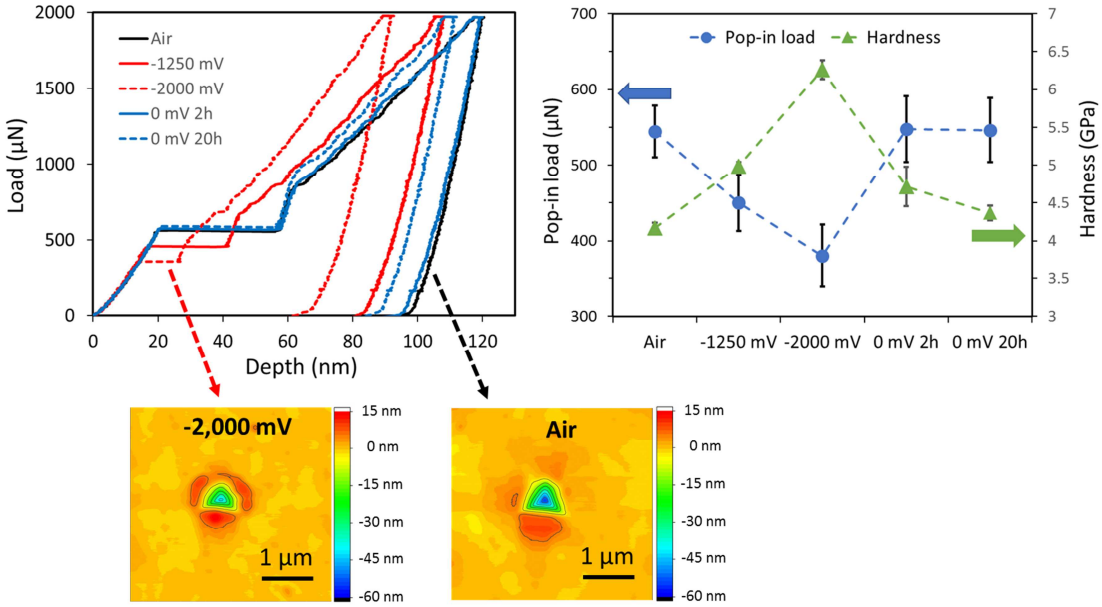

Effect of hydrogen on nanomechanical properties in Fe-22Mn-0.6C TWIP steel revealed by in-situ electrochemical nanoindentation

Dong Wang [a], Xu Lu [a], Yun Deng [a], Xiaofei Guo [b], Afrooz Barnoush [a]

[a] Department of Mechanical and Industrial Engineering, Norwegian University of Science and Technology, Richard Birkelands vei 2B, N-7491 Trondheim, Norway

[b] Steel Institute, RWTH Aachen University, Intzestraße 1, 52072 Aachen, Germany

Corresponding author 1: Afrooz Barnoush
Email: Afrooz.barnoush@ntnu.no
Tel: +47 73593807
Address: Department of Mechanical and Industrial Engineering, Norwegian University of Science and Technology, Richard Birkelands vei 2B, N-7491 Trondheim, Norway

Corresponding author 2: Dong Wang
Email: dong.wang@ntnu.no
Tel: +47 92258324
Address: Department of Mechanical and Industrial Engineering, Norwegian University of Science and Technology, Richard Birkelands vei 2B, N-7491 Trondheim, Norway

Abstract

In-situ electrochemical nanoindentation was applied to study the effect of hydrogen on the mechanical properties of Fe-22Mn-0.6C TWIP steel at the nanoscale. Distinctive behaviors in three defined grain orientations: (001), (101), and (111) were investigated in a sequence of air, hydrogen ingress, and hydrogen egress processes. The obvious pop-in load drop caused by introducing hydrogen was analyzed using the classical dislocation theory in combination with the "Defactant" model, wherein hydrogen-enhanced homogenous dislocation nucleation through the reduction of the dislocation line energy and the stacking fault energy were proposed as the reasons. The dependence of pop-in behaviors on the crystallographic orientations was also discussed. Tabor relation-based models were applied to analyze the nanohardness increment, which was related to the hydrogen-enhanced lattice friction and the hydrogen-reduced plastic zone size. The different recovery behaviors of the pop-in load and nanohardness during hydrogen egress were assessed according to the different amounts of residual hydrogen in the corresponding affected zone.

Keywords: Hydrogen embrittlement; Electrochemical nanoindentation; TWIP steel; Dislocation nucleation; Nanohardness.

1. Introduction

High-Mn twinning-induced plasticity (TWIP) steels have been intensively studied for years owing to their outstanding mechanical properties, including high strength and good ductility [1, 2]. With a pure austenite microstructure, the main strengthening mechanisms of TWIP steels consist of both plasticity-induced dislocation slip and the twinning effect due to their low stacking fault energy (SFE) [3-5]. Therefore, TWIP steels are promising material for cold-forming components in the automotive industry and other energy-related infrastructures. However, this steel is susceptible to unexpected mechanical degradation when exposed to hydrogen-containing environments owing to hydrogen embrittlement (HE) [6-8], which is in accordance with the concept of hydrogen-induced degradation of metals with a transition from ductile to brittle behavior [9]. Although substantial research has been performed to elucidate the mechanism of hydrogen-induced premature failure, no consensus has been reached. Several mechanisms, including hydrogen-enhanced decohesion (HEDE), hydrogen-enhanced localized plasticity (HELP), adsorption-induced dislocation emission (AIDE), and the “Defactant” model, have been proposed according to microscopic observations.

The HEDE mechanism, which was proposed by Troiano [10], involves the accumulation of dissolved hydrogen atoms at trapping sites such as cracks or interfaces, which reduces the cohesive energy of atomic planes or grain boundaries. When the applied stress exceeds the cohesive stress, cracks occur and propagate, resulting in cleavage failure [11, 12], which is widely accepted for explaining intergranular fracture [13, 14]. The HELP mechanism is primarily based on in-situ environmental transmission electron microscopy (TEM) observations of the enhanced dislocation motion and the decreased dislocation interactions in hydrogen-charged samples [15-17]. The enhanced dislocation mobility causes material softening, which is supported by observations of the reduction of the yield stress and flow stress in hydrogenated materials through tensile test [18, 19]. The subdued dislocation interactions are explained by the shielding effect of hydrogen, which facilitates planar slip and promotes pile-up phenomena based on the elastic theory [20, 21]. Besides, the HELP mechanism is also supported by the appearance of quasi-cleavage fracture and surface slip line rearrangement in hydrogen charged samples [22-25]. It is further proved by atomistic simulation [26], and thermodynamic calculations [27-29]. However, contradictory results showing the increase of the flow stress due to the presence of

hydrogen are common in aluminum alloys and austenitic steels at high strain levels [30, 31]. Similarly, hydrogen hardening effect were also reported in bcc iron through both experimental and simulation work [32-35]. Moreover, Song and Curtin proposed that hydrogen provides no shielding effect for dislocation interactions and even weakens the dislocation mobility instead of facilitating it, which is consistent with the solute drag theory based on atomic simulations [36, 37]. The AIDE theory states that the dislocation formation energy is reduced by hydrogen at the crack tips and that the crack propagation is therefore enhanced by easier dislocation emission from the crack tip at relatively low stresses [38, 39]. The “Defactant” concept, which relies on thermodynamics, involves the reduction of the formation energy of defects (such as dislocations) in the presence of defactant solutes, such as hydrogen [27, 28, 40, 41]. In fact, HE is a complex process depending heavily on the material and environment, no aforementioned mechanisms can apply exclusively. For example, in the process of hydrogen-induced crack propagation, dislocations first nucleate at the crack tip based on AIDE and then steady move away due to the enhanced mobility according to HELP [42]. Furthermore, these mechanisms are not completely distinct but with some overlap between each other. AIDE and “Defactant” contain aspects that are also described in HELP is a case in point [29, 39]. To date, most studies on TWIP steels have been dedicated to understanding the mechanisms of HE by altering the alloying elements, microstructure, and testing parameters. As the most common alloying element in TWIP steels, aluminum was proven to improve the resistance to hydrogen delayed fracture by forming an aluminum oxide layer during electrochemical charging, which prevents hydrogen absorption [43]. The addition of aluminum was also reported to enhance the resistance to HE by reducing the hydrogen mobility [33]. However, controversial results showed that aluminum addition has a beneficial effect only in high-strain rate tensile tests, while it is detrimental and promotes crack formation during low-cycle fatigue tests [34]. Copper was reported to have a similar effect to aluminum, while titanium had a negative effect on the HE resistance [44, 45]. Grain refinement was also proposed as a method for enhancing the resistance to HE in TWIP steels by suppressing the ductile-to-brittle transition through the reduction of twin-related boundaries and junctions [46]. In addition, the effect of the strain rate on the HE was analyzed for pre-charged TWIP steels, revealing that the HE becomes more pronounced at a lower strain rate, which enhances the twin-slip interaction by thinning the twins and results in quasi-cleavage fracture [47]. Most investigations focused on macroscopic mechanical testing, which reflects the combined effects of

different lattice defects, whereby it is difficult to clarify the intrinsic influence of dislocations, stacking faults, twinning nucleation, etc. Therefore, investigation at the microscale is needed for a better understanding of the degradation process. Recently, the in-situ hydrogen charging technique showed advantages in studying the HE behavior by eliminating the hydrogen diffusion during tests, especially for body-centered cubic metals that have a high hydrogen diffusion rate [6, 7]. Therefore, it is necessary to integrate in-situ hydrogen charging into the microscale testing. The electrochemical nanoindentation (ECNI) technique, which was proposed by Barnoush [48], has proven to be suitable for probing the hydrogen effect on the mechanical properties of metals in-situ [49, 50]. With the recorded high-resolution load–displacement (L-D) data, not only can the mechanical properties, such as the Young's modulus and nanohardness, be calculated, but also the discrete events, including dislocation nucleation and phase transformation, can be detected in the process of hydrogen charging [49, 51]. In the present study, ECNI tests were performed within single crystals with three defined grain orientations: (001), (101), and (111) to understand the effects of hydrogen absorption and desorption on the mechanical behaviors of TWIP steel and the associated HE mechanisms.

2. Experimental

2.1 Materials and sample preparation

The studied material was Fe-22Mn-0.6C (wt. %) TWIP steel with the chemical composition shown in Table 1. The material was ingot casted, hot rolled, and cold rolled to a thickness of 1.0 mm, followed by grain growth annealing at 1,150 °C for 5 h in an argon atmosphere. The samples used for the ECNI tests were cut via electrical discharge machining into discs with a diameter of 12 mm. The samples were ground sequentially using 220–4,000 grit SiC papers and then polished to 1 μm, followed by additional polishing with a 40-nm colloidal silica suspension for 20 min to remove the deformation layer. The surface quality was checked by using the scanning mode of the nanoindenter, and the final surface root-mean-square roughness was <1 nm over 64 μm^2.

Table 1

Chemical composition of the investigated Fe-22Mn-0.6C TWIP steel

The microstructure of the studied material was analyzed using a high-resolution scanning electron microscope (SEM, Quanta FEG 650 ESEM, FEI Inc.) with a backscatter electron (BSE) detector. Fig. 1(a) shows the microstructure of the tested material, which consisted of grains with an equiaxed morphology and annealing twins. The electron backscatter diffraction (EBSD) technique was used to eliminate the influence of different grain orientations by choosing three defined grains with orientations close to (001), (101), and (111) (i.e. [001], [101], [111] // ND, respectively) as shown in the normal direction-inverse pole figure (ND-IPF) in Fig. 1(b). The measured Euler angles (Bunge definition) of the chosen grains are (41°, 2°, 46°), (88°, 92°, 47°), and (11°, 52°, 46°), respectively, which meet the aforementioned orientation expectations. These ND orientations are also the uniaxial indentation directions during the tests. For simplicity and more explicit description, only Miller indices are used hereafter. The studied material had an average grain size of 85 μm, which was large enough for performing repeated ECNI tests under all charging conditions within a single grain to exclude the influences of the grain size and grain orientation.

Fig. 1. (a) BSE image showing the microstructure of the investigated sample. (b) ND-IPF map of the tested sample with marked (001), (101), and (111) grains.

2.2 Polarization curve

To determine the appropriate charging potentials for the ECNI tests, the polarization curve was measured before the ECNI tests. The electrolyte used for the polarization curve measurement and the following in-situ ECNI test was a glycerol-based solution. The solution consisted of 600 g of Borax (sodium tetraborate decahydrate) dissolved in 1 L of glycerol and diluted with 20% distilled water [52]. In addition, 0.002 M $Na_2S_2O_3$ was added to promote hydrogen absorption [53]. The extremely low solubility and diffusivity of oxygen in the developed electrolyte gave it the advantage of preserving the surface integrity throughout the ECNI test. A three-electrode electrochemical cell consisting of a platinum counter electrode and a $Hg/HgSO_4$ reference electrode was built. Additional details regarding the in-situ setup are presented in Ref. [41]. The polarization curve was measured with a scanning rate of 1 mV/s from -2,500 to 1,000 mV.

The polarization curve is presented in Fig. 2(a), with three chosen potentials highlighted by horizontal dashed lines. The sample exhibited cathodic behavior from -2,500 to -1,100 mV, where hydrogen was produced as the main reaction and diffused into the material. A more

negative cathodic potential resulted in a higher current density. The anodic branch started when the potential was higher than -1,100 mV, where a passive region between -500 and 500 mV was obtained. In this test, -1,250 and -2,000 mV were chosen as cathodic polarization potentials to charge the sample, and 0 mV was chosen as the anodic potential, at which hydrogen diffused out but the sample surface could be kept free of corrosion.

2.3 In-situ ECNI test

In-situ ECNI tests were performed using Hysitron Tribo-Indenter TI 950 with a Berkovich diamond tip, which was also used to scan the sample surface after each group of indentations. The surface topography images were analyzed using Gwyddion software to trace the change of the surface roughness.

The sample was first tested in air, followed by a sequence of -1,250 and -2,000 mV cathodic charging and 0 mV anodic discharging. Before ECNI tests at each cathodic potential, the sample was charged for 2 h for enough hydrogen to be absorbed into the sample. During anodic discharging, the indentations were performed after 2 and 20 h to capture the time-effect of the nanomechanical properties. At least 27 indentations were performed in each condition to guarantee the reproducibility of the results.

The load function used for the test is shown in Fig. 2(b). It consists of a loading segment with an 8,000 μN/s loading rate until the peak load of 2,000 μN is reached, with a holding time of 0.45 s, followed by an 8,000 μN/s unloading segment until 10% of the peak value is reached, with holding for 0.25 s for drift correction.

Fig. 2. (a) Polarization curve of the investigated TWIP sample. The horizontal dashed lines represent the chosen potentials for the ECNI tests. (b) Curve of the load function used for the test.

2.4 Electron channeling contrast imaging (ECCI)

After the nanoindentation (NI) test, the sample was carefully cleaned with distilled water and ethanol. Postmortem analysis was performed using an SEM via the ECCI technique. ECCI has been established as an excellent SEM method based on the controlled diffraction condition with an enhanced contrast [4, 54]. It allowed us to examine the complex deformation microstructure and crystal defects, such as dislocations and stacking faults within the visibility depth below the surface of the metallic materials. In this test, ECCI observations were used to probe the plastic

zone produced by the NI test. The test was performed at an acceleration voltage of 30 kV with a working distance of 6 mm, and the sample was properly tilted to a certain angle to obtain a good channeling condition according to the EBSD adjustment.

3. Results

3.1 Hydrogen effect on nanomechanical properties

The representative L-D curves of the tested grains under different testing conditions are shown in Figs. 3(a)–3(c). All the L-D curves in (101) and (111) grains clearly show four stages: initial elastic loading; an excursion in depth (pop-in), which refers to the onset of plasticity due to homogenous dislocation nucleation (HDN); subsequent elastoplastic loading; and elastic unloading. However, the unique multiple pop-in phenomenon is observed in (001) grain in each testing condition, where the higher pop-ins are proven to result from the nucleation of twins [55]. Except for the initial elastic loading, all the loading stages show differences among different testing conditions. A reduced pop-in load and width, as well as hardening behavior, are observed in the cathodic charging conditions, and the alteration becomes more obvious with the increase of the charging potentials. After the potential is switched to 0 mV, fast recovery of the pop-in behavior and steady recovery of the hardness are observed. During the whole test, the surface roughness that was continuously inspected exhibited no alteration, as shown in Figs. 3(d)–3(g). Therefore, the observed changes of the mechanical properties under different conditions were not due to the change in the surface condition by the electrolyte, but rather due to the dissolved hydrogen.

Fig. 3. Representative L-D curves for (a) (001) grain, (b) (101) grain, and (c) (111) grain tested in air, under two charging conditions and two anodic conditions. (d–g) Representative topographies after indentation in (d) air and at (e) -1,250 mV, (f) -2,000 mV, and (g) 0 mV (after 20 h) in (101) grain.

In the case of pop-in load, which indicates the onset of plasticity, the effects of hydrogen for each grain orientation are detailed in Figs. 4(a) and 4(b). For (111) grain, the average pop-in load in air was 544 μN, and the pop-in load decreased to 450 μN (reduction of 17.3%) when the sample was cathodically charged at -1,250 mV. The pop-in load further decreased to 380 μN

(reduction of 30.1%) at -2,000 mV. After switching to anodic discharging condition, the average pop-in load recovered to the air-value within 2 h and remained unchanged till 20 h of discharging. The amount of hydrogen dissolved into the material in the processes of cathodic charging and anodic discharging will be discussed in detail in section 4.3. Compared with (111) orientation, the pop-in load for (101) orientation exhibited the same trend during the adsorption and desorption of hydrogen, except with different values and a slightly less pronounced effect of hydrogen. In contrast to the single pop-in in (101) and (111) grains, (001) grain exhibited multiple pop-in behavior. Fig. 4(b) shows the cumulative frequency distribution of the first and second pop-ins in (001) grain. Here, we observe a clear drop in both cases when hydrogen was introduced and a recovery of the pop-in load when the hydrogen was removed.

To further analyze the effect of hydrogen on the mechanical properties of the studied material, the nanohardness of the elastic unloading parts was determined using the Oliver–Pharr method [56]:

$$\mathrm{H} = \frac{P_{max}}{A_c}, \tag{1}$$

where P_{max} is the maximum load during the NI test, and A_c is the projected contact area according to the tip area function and the tip contact depth h_c, which can be calculated as follows:

$$h_c \cong h_{max} - 0.75\frac{P_{max}}{S}. \tag{2}$$

Here, h_{max} is the maximum displacement during the NI test, and S is the stiffness extracted from the initial unloading slope of the L-D curve. Clearly, the hardness is increased by introducing hydrogen under cathodic charging and is increased continuously by increasing the cathodic potential. However, in contrast to the pop-in behavior, which recovers in 2 h with the removal of hydrogen, the hardness recovers gradually, exhibiting a time-effect. Taking (101) grain as an example, the hardness value in air is 3.68 GPa, and it increases by 19.0% to 4.38 GPa and by 46.2% to 5.38 GPa at -1,250 and -2,000 mV, respectively. After switching to anodic discharging for 2 h, the hardness first decreases to 4.27 GPa, which is still 16.0% higher than that in air. It decreases to 3.83 GPa after 20 h of discharging. (001) and (111) grains show the same hardness time-effect.

Fig. 4. Pop-in load of (a) (101) and (111) grains and (b) (001) grain; hardness values (c) under different hydrogen absorption and desorption conditions.

3.2 Microstructure after indentation

The representative electron channeling contrast (ECC) images of the indents that were tested in air and under two charging conditions for (101) grain are shown in Figs. 5(a1)–5(a3) and 5(b1)–5(b3). With the applied electron acceleration voltage and the activated diffraction vector, the visibility depth was theoretically 80–100 nm [57]. The dislocations appear as white curved lines or dots on the dark background, while the stacking faults appear as bright areas with a white straight line on one side, indicating the interaction between the stacking fault plane and the sample surface [54]. In the ECC images, both the dislocations and the stacking faults produced in the NI test are clearly observed. Therefore, the contact radius a_c and the plastic zone radius a_{pz} can be estimated. According to a finite-element simulation [58], the plastic zone is designated as the area with more than 1%–2% plastic strain. Thus, the single dislocations or stacking faults that reside far away from the indent center are precluded owing to their negligible effect on the material strength. This is also proved by Choi et al. [59] suggesting that the area of highest dislocation densities used for counting the plastic zone is measured up to a radius approximately half as large as the radius of the total dislocation area. Magnified images of the highlighted indents are shown in Figs. 5(b1)–5(b3), where the radius of the solid circles is a_c and the radius of the dashed circles is a_{pz}. According to our measurement, the average sizes of both a_c and a_{pz} were reduced after electrochemical charging. The effect of hydrogen on the plasticity zone size can be expressed by the ratio of a_{pz} to a_c, which was calculated as 1.63, 1.52, and 1.40 in air and at -1,250 and -2,000 mV, respectively, showing that the plastic zone area detected via ECCI was reduced in the presence of hydrogen. The localized plasticity is also indicated by the topography and pile-up. Figs. 5(c1)–5(c3) present the two-dimensional (2D) color-filled contour images for different charging conditions, and Figs. 5(d1)–5(d3) show the height data for the three dashed lines in Figs. 5(c1)–5(c3). The height of the pile-ups increased from 10 nm in air to 13 and 15 nm in -1,250 and -2,000 mV cathodic charging conditions, respectively. Normally, in a load-controlled NI test, the total deformation is reflected by the summation of the plastic zone and pile-up. Additionally, the deformation degree should be proportional to the maximum indentation depth. Fig. 3(b) shows that the maximum indentation depth in (101) grain was smaller in cathodic charging condition than in air or anodic charging condition, which indicates

less deformation in the presence of hydrogen. Thus, more pile-ups in the charging condition confirmed more pronounced shrinkage of the plastic zone surrounding the indents. The more confined plastic zone in the hydrogen charging condition proves that hydrogen dragged dislocation motion and restricted the dislocation cross slip due to the enhanced slip planarity in the frame of the HELP mechanism.

Fig. 5. Groups (a) and (b) contain ECC images of the representative indents. Group (b) contains magnified images of the indents indicating the contact area and the plastic zone. Group (c) contains the 2D color-filled contour plots showing the surface topography, and group (d) contains plots of the related pile-up data. The numbers (1), (2), and (3) represent the different testing conditions: air, -1,250 mV, and -2,000 mV, respectively. All the images are for the (101) grain.

4 Discussion

4.1 Hydrogen effect on dislocation and twin nucleation

To understand the effect of hydrogen on the elastic behavior of the material, the Hertzian contact theory was applied to model the elastic interactions between the indenter and the surface [60]:

$$\mathrm{P} = \frac{4}{3} E_r \sqrt{R h^3} \ , \tag{3}$$

where P is the applied load, h is the indentation depth, R is the radius of the tip curvature, and E_r is the reduced modulus. According to the Oliver–Pharr method [56], the reduced modulus can be measured by analyzing the elastic unloading part of the L-D curve, as follows:

$$E_r = \frac{\sqrt{\pi}}{2} \frac{1}{\beta} \frac{S}{\sqrt{A_c}}, \tag{4}$$

where β is a correction factor based on the geometry of the indenter tip (1.034 for Berkovich indenter). Using the calculated E_r values, it is possible to estimate the radius of the tip curvature by applying the Hertzian fit according to Eq. (3). In the present study, the Berkovich tip radius was 1.0 μm.

According to the contact mechanics, the elastic loading starts from the contact between the tip and the surface until the first dislocation nucleation and motion occur, which indicates the onset of plasticity [41, 60]. For an annealed metallic material, the typical dislocation density is in the

range of 10^{10}–10^{14} m^{-2}, which means that dislocations are separated by 1–10 μm. Because the elastic region probes a depth of approximately 20 nm before the occurrence of pop-in phenomena, as shown in Fig. 3, the indented volume in the elastic area is 100 times smaller than the average dislocation space. Thus, it is reasonable to assume that the areas where the indents are performed contain no pre-existing dislocations. The absence of pre-existing dislocations means that the elastic loading continues until the shear stress beneath the tip reaches the theoretical shear stress, where the HDN occurs with the pop-in phenomena, followed by subsequent dislocation gliding and other motion events [49, 60].

According to the classical dislocation theory [61], the free energy required to form a dislocation loop with a radius of r is described as

$$\Delta G = 2\pi r W_{dis} + \pi r^2 \gamma - \pi r^2 b \tau_{max}, \tag{5}$$

where W_{dis} is the line energy of the newly formed dislocation loop, γ is the SFE, which is 0.023 J/m^2 for the studied steel [59], and b is the Burgers vector of partial dislocation (0.15 nm) [5]. The term $2\pi r W_{dis}$ represents the line energy of the whole dislocation loop, the term $\pi r^2 \gamma$ represents the formation energy of a stacking fault, and the last term represents the work needed for expanding the dislocation loop.

For visualizing the energy needed to generate a dislocation loop, the maximum shear stress τ_{max} for HDN [62, 63] and the line energy W_{dis} of a circular dislocation loop in an infinite isotropic elastic solid [61] can be obtained as follows:

$$\tau_{max} = 0.31 \left(\frac{6E_r^2}{\pi^3 R^2} P \right)^{\frac{1}{3}} \tag{6}$$

$$W_{dis} = \frac{2-\upsilon}{1-\upsilon} \frac{\mu b^2}{8\pi} \left(\ln \frac{4r}{\psi} - 2 \right), \tag{7}$$

where υ is the Poisson's ratio (0.27), μ is the shear modulus, and ψ is the dislocation core radius ($\sim \frac{b}{2}$). The shear modulus μ can be calculated using the Poisson's ratio υ and the elastic modules E as follows: $\mu = E/2(1+\upsilon)$. The elastic modulus is given by

$$\frac{1}{E_r} = \frac{1-\upsilon_1^2}{E_1} + \frac{1-\upsilon_2^2}{E_2}. \tag{8}$$

Here, the subscripts 1 and 2 represent the sample and the tip, respectively. For a diamond tip, the elastic modulus is 1,140 GPa, and the Poisson's ratio is 0.07. By combining Eqs. (6) and (7), the free energy of dislocation loop formation can be expressed as

$$\Delta G = \frac{2-\upsilon}{1-\upsilon}\frac{\mu b^2 r}{4}\left(\ln\frac{4r}{\psi}-2\right)+\pi r^2\gamma-\pi r^2 b\tau_{max}\,. \tag{9}$$

Fig. 6 shows the free energy of HDN as a function of the dislocation loop radius in different charging conditions for the defined orientations. All the free-energy curves pass through a maximum value ΔG^* at the critical loop radius r^*, where ΔG^* is defined as the activation energy for HDN and can be calculated by setting $\frac{\delta \Delta G}{\delta r}=0$. To obtain a stabilized dislocation loop, the activation energy must overcome the energy barrier, ΔG^* in this case, for the dislocation to grow larger than r^*. It was reported that the available thermal energy at room temperature is 0.0026 eV [41]. Therefore, the dislocation loop is nucleated spontaneously and the pop-in can be observed only for a maximum free energy ΔG^* lower than 0.0026 eV. This is exactly what occurred during the NI test in the air and anodic conditions. When the sample was charged with hydrogen, the calculated ΔG^* was significantly higher than 0.0026 eV in all cases. According to the previous thermodynamic assumptions, the dislocation loop is not supposed to nucleate. Nonetheless, all the recorded L-D curves for the cathodic conditions clearly exhibit pop-in phenomena, which means that the existing energy barriers at the cathodic potentials were somehow overcome by the dissolved hydrogen. This can be explained by the "Defactant" model, which proposes that hydrogen can reduce the formation energy of defects, such as dislocations and stacking faults, and enhance the defect formation [27, 28, 40]. For a linear dislocation, the hydrogen segregation around the dislocation line can effectively increase the dislocation core radius [64, 65], reducing the line energy of the dislocation according to Eq. (7). The reduction of the SFE by hydrogen has been demonstrated via both experiment and simulation [66, 67]. Therefore, the dissolved hydrogen results in easier formation of the dislocation loop and stacking fault during NI, which is reflected by the reduction of the pop-in load in the L-D curves. This defect-reduction phenomenon becomes more pronounced with more absorbed hydrogen, as shown in Fig. 4.

Fig. 6. Free energy of HDN with respect to the dislocation loop radius (r) for (001) (a), (101) (b), and (111) (c) grain orientations. The activation energy for HDN ($\Delta G^{\star}$) and the critical loop radius ($r^{\star}$) in the -2,000 mV charging condition are shown in (c).

Additionally, the crystallographic orientation is an important factor determining the mechanical properties and deformation behaviors of crystalline alloys. According to Fig. 4, the orientation-dependent pop-in behaviors can be summarized as follows. 1) The L-D curves in (001) grain are more complicated with multiple pop-ins. 2) The average pop-in load in (111) grain is higher than that in (101) grain under all testing conditions. The orientation dependence of the uniaxial yield stress can be expressed by the variation of Schmid factors in different slip planes. Normally for a tensile test, the slip system with the largest Schmid factor experiences the highest shear stress and will be activated first when the critical shear stress is reached. Although the stress state beneath the indenter is not comparable to the uniaxial tensile test due to the complexity below the indenter tip, it is reasonable to consider the indentation process as an uniaxial compression for simplicity [68] and use Schmid factor to help understanding the dislocation slip behavior in each grain orientation. The maximum Schmid factors for dislocation slip system {111}<110> and mechanical twinning system {111}<112> are presented in Table 2 [69]. The Schmid factor for mechanical twinning in (001) grain is approximately two times higher than that for (101) and (111) grains; thus, mechanical twinning occurs more easily. Considering the multiple pop-in behavior in (001) grain, it is reasonable to propose that the second and subsequent pop-ins are related to the nucleation of deformation twins. It needs to mention here that mechanical twinning can only occur after the activation of multiple slip systems although the highest Schmid factor for twinning is larger than that for slip as in (001) grain [70, 71]. Gutierrez-Urrutia et.al. [72] reported the evidence in TWIP steel that once multiple slip is activated, twinning occurs readily. Furthermore, the association between the pop-ins and deformation twins in TWIP steel was also proposed by Misra [55], who performed TEM analysis indicating that the first pop-in is nucleation of dislocation, while subsequent pop-ins are related to deformation twinning. For (101) and (111) grains, with lower Schmid factors for mechanical twinning compared with that for slip, dislocation slip is more favorable, which results in single pop-ins on L-D curves, indicating dislocation nucleation. However, the Schmid factor for dislocation slip is 0.41 in (101) grain, which is 1.464 times higher than that in (111) grain (0.28). Therefore, the critical resolved shear stress for slip is expected to be reached earlier with a lower pop-in load in (101) grain than in

(111) grain. According to the data in Fig. 4, the average pop-in loads in air are 373.16 GPa in (101) grain and 544.41 GPa in (111) grain, differing by a factor of 1.459, which perfectly matches the ratio of their Schmid factors.

Table 2
Maximum Schmid factors of different orientations under compression for preferred dislocation slip system {111}<110> and mechanical twinning system {111}<112> [69]

4.2 Hydrogen effect on lattice friction

As shown in Fig. 3, the dissolved hydrogen not only reduces the pop-in load but also influences the elastoplastic part of the L-D curves, with a hardening effect. To elucidate this effect, the models developed by Nix-Gao and Durst are introduced [73, 74]. The elastoplastic curve can be described by the models according to the Tabor relation:

$$\mathrm{P} = \mathrm{H}_0 A_c \,, \tag{10}$$

where A_c is the contact area used in Section 3.1, and H_0 is the depth-independent hardness of the material obtained from the NI test, which can be expressed as follows.

$$\mathrm{H}_0 = \mathrm{C}\sigma \,. \tag{11}$$

Here, C is the Tabor factor transforming the complex stress state beneath the indenter into a uniaxial stress state [60]. In the current study, the Tabor factor C is assumed as 3 [75]. Because the NI test was performed on defined grains that can be treated as a single crystal, the hardening mechanisms induced by the grain boundaries and phase boundaries are ignored. Hence, the stress σ is assumed to be influenced only by the lattice friction (σ_{Fric}) and the interaction between dislocations, which is described as Taylor stress (σ_{Taylor}). W. S. Choi et al. [59] found that the lattice friction stress σ_{Fric} in polycrystalline Fe-22Mn-0.6C TWIP steel was 242 MPa by considering the solid solution strengthening effect. The Taylor stress (σ_{Taylor}) is described by the Taylor relation [74]:

$$\sigma_{Taylor} = M\alpha\mu b\sqrt{\rho_{dis}} \,, \tag{12}$$

where M is the Taylor factor, which is reported to be 3.06 [59], and α is an empirical factor depending on the dislocation structure. Owing to the complex stress field beneath the indenter, a constant value of $\alpha = 0.5$ is chosen [73]. The dislocation density ρ_{dis} consists of the statistically

stored dislocation (SSD) density, ρ_{SSD}, and the geometrically necessary dislocation (GND) density, ρ_{GND}. For our annealed sample with a deformation-free surface, it is reasonable to assume that the ρ_{SSD} value is 10^{12} m^{-2}. GNDs are accumulated in strain gradient fields caused by geometrical constraints of the crystal lattice, and the density is described according to the Nix-Gao model [74]:

$$\rho_{GND} = \frac{3}{2}\frac{1}{f^3}\frac{\tan^2\theta}{bh}, \tag{13}$$

where θ is the angle between the sample surface and the indenter, which is 24.63° for the Berkovich tip, and f is the ratio of the plastic zone radius to the contact area radius (a_{pz}/a_c) described in Section 3.2. By combining Eqs. (10)–(13), the elastoplastic regime can be described as follows.

$$\mathrm{P} = \mathrm{CM}\alpha\mu\mathrm{b}A_c\sqrt{\rho_{SSD} + \frac{3}{2}\frac{1}{f^3}\frac{\tan^2\theta}{bh}} + \mathrm{C}\sigma_{Fric}A_c\,. \tag{14}$$

The results are shown in Fig. 7, where the fitting curves obtained using Eq. (14) by inserting the f value of 1.63 obtained from Section 3.2 are fully consistent with the experimental data obtained in air. To explain the hydrogen effect on the elastoplastic regime, we assume that the dissolved hydrogen has an influence on both σ_{Fric} and σ_{Taylor}. As mentioned previously, the electrochemical hydrogen charging process was performed such that the formation of defects was avoided. Therefore, it is reasonable to assume that the dissolved hydrogen has no effect on ρ_{SSD} but influences σ_{Fric} and ρ_{GND}. Eq. (14) can therefore be rearranged as

$$\mathrm{P} = \mathrm{CM}\alpha\mu\mathrm{b}A_c\sqrt{\rho_{SSD} + \frac{3}{2}\frac{1}{{f_H}^3}\frac{\tan^2\theta}{bh}} + \mathrm{C}(\sigma_{Fric} + \sigma_H)A_c\,, \tag{15}$$

where σ_H is the contribution of the dissolved hydrogen to the lattice friction, and f_H is the hydrogen-affected ratio of the plastic zone radius to the contact radius, which can be obtained from the ECCI results in Section 3.2. The value of σ_H can be quantitatively calculated by fitting the experimental data in the hydrogen-charged condition using Eq. (15). The fitted σ_H values in different conditions together with the most relevant parameters used for the simulation are presented in Table 3. In the case of (101) grain orientation, with the introduction of hydrogen,

the lattice friction shows an increment of 45 MPa at -1,250 mV and increases to 210 MPa at -2,000 mV. The same trend is observed for (111) grain orientation, with values of 75 and 340 MPa, respectively. The lattice friction in (001) grain cannot be determined, owing to the limited elastoplastic part with multiple pop-ins, which makes it difficult to fit using Eq. (15). Regardless, it is reasonable to infer that the increment of the lattice friction is due to the interactions between dislocations and dissolved hydrogen atoms. Because the depth of indents is limited to ~100 nm, the dissolved hydrogen in this area is sufficient to generate Cottrell atmospheres around the moving dislocations, resulting in a resistance to dislocation motion, which is consistent with the solute drag theory [61]. This idea is supported by the atomistic simulation results of Song and Curtin [37]. Therefore, the hardening effect of hydrogen can be explained by the increment of the lattice friction and the reduction of f. A larger amount of hydrogen generated by adjusting the cathodic potential yielded a more pronounced hardening effect, as shown in Fig. 4(c).

Fig. 7. Typical L-D curves of the (a) (101) grain and (b) (111) grain obtained in air and different H-charging conditions. The elastic regimes are fitted by Hertzian model. The elastoplastic parts are modeled according to Eqs. (14) and (15).

Table 3
Sets of parameters used for modeling the L-D curves

4.3 Anodic time-effect on nanohardness

The results in Fig. 4 show the unambiguous effect of hydrogen on the pop-in behavior and the hardness of TWIP steel. Generally, with dissolved hydrogen, the pop-in load decreases and the hardness increases. However, an interesting feature is observed when the hydrogen desorption begins. With anodic charging for 2 h, the pop-in loads recover to values that are consistent with the data obtained in air (Figs. 4(a) and 4(b)). In contrast, the hardness recovers slowly, exhibiting a time-effect (Fig. 4(c)): after 2 h of discharging, the hardness for (001), (101), and (111) grain orientations show only 68.4%, 65.3%, and 73.8% recovery, and after 20 h of discharging, the hardness values recover by 88.3%, 91.6%, and 90.5%, respectively. The variation of the recovery behaviors for the pop-in load and hardness is attributed to the different affecting depths beneath the indenter. According to continuum mechanics, the maximum shear stress for pop-in during an NI test occurs below the sample surface, within a distance of 0.48 times the contact radius r_c [60].

The contact radius r_c and the position of the maximum shear stress $Z_{\tau(max)}$ are calculated as follows [76].

$$r_c = \left(\frac{3PR}{4E_r}\right)^{\frac{1}{3}}. \tag{16}$$

$$Z_{\tau(max)} = 0.48 r_c = 0.48\left(\frac{3PR}{4E_r}\right)^{\frac{1}{3}}. \tag{17}$$

By substituting the tip radius of 1 μm, the pop-in load, and the reduced modulus into the above equations, the affected maximum shear stress depth $Z_{\tau(max)}$, which is in the range of 60 ± 3 nm, can be calculated. Therefore, the energy for the onset of dislocation, i.e., the HDN, is determined by the perceptive stress in this depth range.

On the contrary, the hardness response of the sample is determined by the aforementioned lattice friction and the Taylor stress. The hardness is dominated by the plastic zone beneath the indenter. Several models for probing the plastic zone size have been proposed [58, 77, 78]. Among them, the model developed by Lawn et al. [79] relates the plastic zone radius r_{pz} to the residual indentation depth h_f:

$$r_{pz} = \varphi\left(\frac{E}{H}\right)^n tan^{\frac{1}{3}}(\theta) h_f\ , \tag{18}$$

where φ is the geometry constant (3.64 for Berkovich [80]). E is the elastic modulus calculated from the reduced modulus based on Eq. (8). θ takes the same value as in Eq. (13). The constant n was originally suggested to be 1/2 and was optimized as 1/3 [81]. By substituting the calculated $\frac{E}{H}$ values in different conditions, r_{pz} is calculated in the range of 835 ± 25 nm. Notably, the radius of the plastic zone measured from the ECC images is between 790 and 877 nm, which agrees with the Lawn model. Therefore, during the ECNI tests, the dissolved hydrogen depth influencing the hardness was significantly larger than that affecting the pop-in load.

To further analyze the variation of the hydrogen concentration during charging and discharging, Fick's law is used to describe the diffusion process beneath the sample surface. During cathodic charging, the exit side of the sample has marginal or no influence on the hydrogen concentration. We can consider the diffusion process by using "the thick plate solution" model [82]:

$$\frac{C(x,t)-C_0}{C_i-C_0}=1-\mathrm{erf}\left(\frac{x}{\sqrt{4Dt}}\right) \tag{19}$$

$$\mathrm{erf}(u)=\frac{2}{\sqrt{\pi}}\int_0^u \exp(-u^2)\,du\,, \tag{20}$$

where $C(x,t)$ is the concentration of hydrogen in the sample, C_i is the constant surface hydrogen concentration, C_0 is the uniform initial bulk hydrogen distribution, and D is the hydrogen diffusion coefficient, which is chosen as $1.8\times10^{-16}\ m^2/s$ in accordance with Ref. [82].

For simplicity, we assume the surface hydrogen concentration to be a constant value C_s for all the charging conditions and assume the initial bulk hydrogen concentration to be 0. The results are presented by the ratio of $C(x,t)$ to C_s. Therefore, after 12 h (43,200 s) of cathodic charging in the NI test, the hydrogen concentration in the sample can be expressed as follows.

$$\frac{C(x,43{,}200s)}{C_s}=1-\mathrm{erf}\left(\frac{x}{\sqrt{4Dt}}\right) \tag{21}$$

In the case of hydrogen desorption during anodic discharging, the situation is more complex, owing to the non-constant initial hydrogen concentration beneath the sample surface, which does not fulfill the boundary conditions of Eq. (19). Therefore, the non-steady state equation with a constant surface concentration and initial distribution $f(x)$ is used [83]:

$$\begin{aligned}C(x,t)=C_1+(C_2-C_1)\frac{x}{l}+\frac{2}{\pi}\sum_1^\infty\frac{C_2\cos n\pi-C_1}{n}\sin\frac{n\pi x}{l}\exp\left(-\frac{Dn^2\pi^2t}{l^2}\right)\\ +\frac{2}{l}\sum_1^\infty\sin\frac{n\pi x}{l}\exp\left(-\frac{Dn^2\pi^2t}{l^2}\right)\int_0^l f(x')\sin\frac{n\pi x'}{l}dx'\,,\end{aligned} \tag{22-1}$$

where

$$C=C_1,\quad x=0,\quad t\geq0, \tag{22-2}$$

$$C=C_2,\quad x=l,\quad t\geq0, \tag{22-3}$$

$$C=\frac{C(x,43{,}200s)}{C_s}=1-\mathrm{erf}\left(\frac{x}{\sqrt{4Dt}}\right),\quad 0<x<l,\quad t=0\,. \tag{22-4}$$

According to the foregoing models, the hydrogen concentration distribution in each condition is schematically shown in Fig. 8. After cathodic charging, a hydrogen concentration gradient

clearly exists beneath the surface, as indicated by the red line. At the beginning of the discharging, we assume the boundary condition $C_1 = 0$ at the sample surface ($x = 0$) and $C_2 = 0$ at the depth of 10,000 nm, according to the cathodic curve highlighted by the red line in Fig. 8. In accordance with Eq. (22), the calculated hydrogen concentrations after 2 and 20 h (7,200 and 72,000 s) of anodic discharging are indicated by the black dashed line and black solid line in Fig. 8, respectively.

With reference to the constant surface hydrogen concentration C_s, the sample is deemed to be saturated with hydrogen at the depth of 60 ± 3 nm during electrochemical charging, which corresponds to the depth controlling the pop-in load. On the other hand, the hydrogen concentration at the depth of 835 nm, which significantly affects the hardness, reaches 83.1% C_s. It has been concluded that the dissolved hydrogen at the aforementioned two depths leads to the reduction of the pop-in load and the increase of the hardness. After 2 and 20 h of discharging, the dissolved hydrogen is almost imperceptible at the depth of 60 ± 3 nm. Therefore, pop-in loads obtained at two anodic discharging conditions are both controlled by a hydrogen-free region leading to the same pop-in load as in air. However, there is still 24.3% C_s hydrogen left at the depth of 835 nm after 2 h of discharging, as shown in Fig. 8. This means that 29.2% of the pre-existing hydrogen (considering the original hydrogen concentration to be 83.1% C_s) in this depth range remains, resulting in a hardening effect and delayed hardness recovery. According to the data shown in Table 4, the concentration of the remaining hydrogen (29.2%) fits perfectly with the calculated percentage of hardness recovery after 2 h of anodic discharging. Moreover, the remaining hydrogen concentration decreases to 3.1% (2.57% C_s) after 20 h, in which case the hardness recovers to 91.6%. Therefore, it can be concluded that the fast recovery of the pop-in load and slow recovery of the hardness in the anodic condition are caused by the different amounts of remaining hydrogen at the corresponding affected depths.

Fig. 8. (a) Hydrogen concentration profiles in different charging and discharging conditions. The red line represents the hydrogen concentration after cathodic charging. The black dashed line and black solid line indicate the hydrogen concentrations after 2 h and 20 h anodic discharging, respectively. (b) Enlarged area in (a) with two blue dotted lines indicating the depths of 63 and 835 nm beneath the sample surface.

Table 4

Correlation between the hardness and the hydrogen concentration at the depth of 835 nm

5. Conclusion

The effect of hydrogen on the nanomechanical properties of Fe-22Mn-0.6C TWIP steel was investigated for three different grain orientations using the in-situ ECNI technique. Changes of the pop-in load and nanohardness were observed in the process of charging and discharging. The effects of hydrogen on the HDN, plastic zone size, and lattice friction were analyzed. The main conclusions are as follows.

1. The introduction of hydrogen reduced the pop-in load, which is attributed to the hydrogen-assisted HDN. The classical dislocation theory was used to calculate the required free energy for the HDN, and the results indicated that the dissolved hydrogen acted as defactant solute and substantially reduced the dislocation formation energy.

2. While single pop-in was observed in (101) and (111) grains, multiple pop-in behavior was detected in (001) grain. The second and subsequent pop-ins in (001) grain are attributed to the nucleation of deformation twins, which is consistent with the high Schmid-factor values for twin nucleation.

3. Under the exposure of hydrogen, enhanced hardening behavior was observed in the elastoplastic region, which increased the nanohardness. This phenomenon was related to the enhanced retarding stress on the dislocation motion caused by the reduced plastic zone size and the increased lattice friction between the dislocations and hydrogen.

4. During anodic discharging, the pop-in load exhibited fast recovery; however, the nanohardness showed a time-effect. Due to their different affecting depths, the discrepancy in the amount of residual hydrogen at corresponding depths explains the different recovery speeds.

Acknowledgements

The authors are grateful for the support provided by the Research Council of Norway through the HyF-Lex (244068/E30) project, the China scholarship council, and the promotion of scientific exchange by the German Research Foundation (DFG) in the framework of the Collaborative

Research Center SFB 761 “Steel - ab initio.” The authors are also thankful to Prof. Jianying He of the Department of Structural Engineering (NTNU) for the helpful discussion.

Reference:

[1] O. Grassel, L. Kruger, G. Frommeyer, L.W. Meyer, High strength Fe-Mn-(Al, Si) TRIP/TWIP steels development-properties-application, Int. J. Plast. 16(10-11) (2000) 1391-1409.
[2] B.C. De Cooman, Y. Estrin, S.K. Kim, Twinning-induced plasticity (TWIP) steels, Acta Mater. 142 (2018) 283-362.
[3] O. Bouaziz, S. Allain, C.P. Scott, P. Cugy, D. Barbier, High manganese austenitic twinning induced plasticity steels: A review of the microstructure properties relationships, Curr. Opin. Solid State Mater. Sci. 15(4) (2011) 141-168.
[4] I. Gutierrez-Urrutia, D. Raabe, Dislocation and twin substructure evolution during strain hardening of an Fe-22 wt.% Mn-0.6 wt.% C TWIP steel observed by electron channeling contrast imaging, Acta Mater. 59(16) (2011) 6449-6462.
[5] D.R. Steinmetz, T. Japel, B. Wietbrock, P. Eisenlohr, I. Gutierrez-Urrutia, A. Saeed-Akbari, T. Hickel, F. Roters, D. Raabe, Revealing the strain-hardening behavior of twinning-induced plasticity steels: Theory, simulations, experiments, Acta Mater. 61(2) (2013) 494-510.
[6] M. Koyama, E. Akiyama, K. Tsuzaki, D. Raabe, Hydrogen-assisted failure in a twinning-induced plasticity steel studied under in situ hydrogen charging by electron channeling contrast imaging, Acta Mater. 61(12) (2013) 4607-4618.
[7] M. Koyama, E. Akiyama, K. Tsuzaki, Hydrogen embrittlement in a Fe-Mn-C ternary twinning-induced plasticity steel, Corros. Sci. 54 (2012) 1-4.
[8] N. Zan, H. Ding, X.F. Guo, Z.Y. Tang, W. Bleck, Effects of grain size on hydrogen embrittlement in a Fe-22Mn-0.6C TWIP steel, Int. J. Hydrog. Energy 40(33) (2015) 10687-10696.
[9] M. Nagumo, Fundamentals of hydrogen embrittlement, Springer, Singapore, 2016.
[10] A.R. Troiano, R. Gibala, R. Hehemann, Hydrogen embrittlement and stress corrosion cracking: a Troiano Festschrift, ASM International, Ohio, 1984.
[11] R.A. Oriani, P.H. Josephic, Equilibrium Aspects of Hydrogen-Induced Cracking of Steels, Acta Metall. 22(9) (1974) 1065-1074.
[12] Y.F. Wang, J.M. Gong, W.C. Jiang, A quantitative description on fracture toughness of steels in hydrogen gas, Int. J. Hydrog. Energy 38(28) (2013) 12503-12508.
[13] Z. Tarzimoghadam, M. Rohwerder, S.V. Merzlikin, A. Bashir, L. Yedra, S. Eswara, D. Ponge, D. Raabe, Multi-scale and spatially resolved hydrogen mapping in a Ni-Nb model alloy reveals the role of the δ phase in hydrogen embrittlement of alloy 718, Acta Mater. 109 (2016) 69-81.
[14] A. Laureys, T. Depover, R. Petrov, K. Verbeken, Influence of sample geometry and microstructure on the hydrogen induced cracking characteristics under uniaxial load, Mater. Sci. Eng. A 690 (2017) 88-95.
[15] D. Shih, I. Robertson, H. Birnbaum, Hydrogen embrittlement of α titanium: in situ TEM studies, Acta Metall. 36(1) (1988) 111-124.
[16] M.L. Martin, P. Sofronis, I.M. Robertson, T. Awane, Y. Murakami, A microstructural based understanding of hydrogen-enhanced fatigue of stainless steels, Int. J. Fatigue 57 (2013) 28-36.
[17] I.M. Robertson, P. Sofronis, A. Nagao, M.L. Martin, S. Wang, D.W. Gross, K.E. Nygren, Hydrogen Embrittlement Understood, Metall. Mater. Trans. A 46a(6) (2015) 2323-2341.
[18] D.F. Teter, I.M. Robertson, H.K. Birnbaum, The effects of hydrogen on the deformation and fracture of beta-titanium, Acta Mater. 49(20) (2001) 4313-4323.

[19] G.M. Bond, I.M. Robertson, H.K. Birnbaum, Effects of Hydrogen on Deformation and Fracture Processes in High-Purity Aluminum, Acta Metall. 36(8) (1988) 2193-2197.
[20] J.P. Chateau, D. Delafosse, T. Magnin, Numerical simulations of hydrogen-dislocation interactions in fcc stainless steels. Part II: hydrogen effects on crack tip plasticity at a stress corrosion crack, Acta Mater. 50(6) (2002) 1523-1538.
[21] H.K. Birnbaum, P. Sofronis, Hydrogen-enhanced localized plasticity—a mechanism for hydrogen-related fracture, Materials Science and Engineering: A 176(1) (1994) 191-202.
[22] M.L. Martin, J.A. Fenske, G.S. Liu, P. Sofronis, I.M. Robertson, On the formation and nature of quasi-cleavage fracture surfaces in hydrogen embrittled steels, Acta Mater. 59(4) (2011) 1601-1606.
[23] T. Neeraj, R. Srinivasan, J. Li, Hydrogen embrittlement of ferritic steels: Observations on deformation microstructure, nanoscale dimples and failure by nanovoiding, Acta Mater. 60(13-14) (2012) 5160-5171.
[24] W.A. Mcinteer, A.W. Thompson, I.M. Bernstein, The Effect of Hydrogen on the Slip Character of Nickel, Acta Metall. 28(7) (1980) 887-894.
[25] E. Lunarska, V. Novak, N. Zarubova, S. Kadeckova, Effect of Electrolytic Hydrogen Charging on Flow-Stress and Slip Line Pattern in Iron Single-Crystals, Scr. Metall. Mater. 17(6) (1983) 705-710.
[26] G. Lu, Q. Zhang, N. Kioussis, E. Kaxiras, Hydrogen-enhanced local plasticity in aluminum: An ab initio study, Phys. Rev. Lett. 87(9) (2001) art. no.-095501.
[27] R. Kirchheim, Reducing grain boundary, dislocation line and vacancy formation energies by solute segregation. I. Theoretical background, Acta Mater. 55(15) (2007) 5129-5138.
[28] R. Kirchheim, Reducing grain boundary, dislocation line and vacancy formation energies by solute segregation II. Experimental evidence and consequences, Acta Mater. 55(15) (2007) 5139-5148.
[29] R. Kirchheim, Revisiting hydrogen embrittlement models and hydrogen-induced homogeneous nucleation of dislocations, Scr. Mater. 62(2) (2010) 67-70.
[30] C. Verpoort, D.J. Duquette, N.S. Stoloff, A. Neu, The Influence of Plastic-Deformation on the Hydrogen Embrittlement of Nickel, Mater. Sci. Eng. 64(1) (1984) 135-145.
[31] D.P. Abraham, C.J. Altstetter, The Effect of Hydrogen on the Yield and Flow Stress of an Austenitic Stainless Steel, Metall. Mater. Trans. A 26(11) (1995) 2849-2858.
[32] M. Itakura, H. Kaburaki, M. Yamaguchi, T. Okita, The effect of hydrogen atoms on the screw dislocation mobility in bcc iron: A first-principles study, Acta Mater. 61(18) (2013) 6857-6867.
[33] T. Depover, E. Wallaert, K. Verbeken, On the synergy of diffusible hydrogen content and hydrogen diffusivity in the mechanical degradation of laboratory cast Fe-C alloys, Mater. Sci. Eng. A 664 (2016) 195-205.
[34] Y. Tobe, W.R. Tyson, Effect of Hydrogen on Yield of Iron, Scr. Metall. Mater. 11(10) (1977) 849-852.
[35] W.B. Xie, X.Y. Liu, W.X. Chen, H. Zhang, Hydrogen hardening effect in heavily deformed single crystal alpha-Fe, Comp. Mater. Sci. 50(12) (2011) 3397-3402.
[36] J. Song, W.A. Curtin, A nanoscale mechanism of hydrogen embrittlement in metals, Acta Mater. 59(4) (2011) 1557-1569.
[37] J. Song, W.A. Curtin, Mechanisms of hydrogen-enhanced localized plasticity: An atomistic study using alpha-Fe as a model system, Acta Mater. 68 (2014) 61-69.
[38] S.P. Lynch, Environmentally Assisted Cracking: Overview of Evidence for an Adsorption-Induced Localized-Slip Process, Acta Metall. 36(10) (1988) 2639-2661.
[39] S. Lynch, Hydrogen embrittlement phenomena and mechanisms, Corros. Rev. 30(3-4) (2012) 105-123.
[40] I.M. Robertson, The effect of hydrogen on dislocation dynamics, Eng. Fract. Mech. 68(6) (2001) 671-692.
[41] A. Barnoush, H. Vehoff, Recent developments in the study of hydrogen embrittlement: Hydrogen effect on dislocation nucleation, Acta Mater. 58(16) (2010) 5274-5285.
[42] O. Barrera, D. Bombac, Y. Chen, T.D. Daff, E. Galindo-Nava, P. Gong, D. Haley, R. Horton, I. Katzarov, J.R. Kermode, C. Liverani, M. Stopher, F. Sweeney, Understanding and mitigating hydrogen

embrittlement of steels: a review of experimental, modelling and design progress from atomistic to continuum, J. Mater. Sci. 53(9) (2018) 6251-6290.
[43] I.J. Park, K.H. Jeong, J.G. Jung, C.S. Lee, Y.K. Lee, The mechanism of enhanced resistance to the hydrogen delayed fracture in Al-added Fe-18Mn-0.6C twinning-induced plasticity steels, Int. J. Hydrog. Energy 37(12) (2012) 9925-9932.
[44] I.J. Park, S.Y. Jo, M. Kang, S.M. Lee, Y.K. Lee, The effect of Ti precipitates on hydrogen embrittlement of Fe-18Mn-0.6C-2Al-xTi twinning-induced plasticity steel, Corros. Sci. 89 (2014) 38-45.
[45] T. Dieudonne, L. Marchetti, M. Wery, J. Chene, C. Allely, P. Cugy, C.P. Scott, Role of copper and aluminum additions on the hydrogen embrittlement susceptibility of austenitic Fe-Mn-C TWIP steels, Corros. Sci. 82 (2014) 218-226.
[46] I.J. Park, S.M. Lee, H.H. Jeon, Y.K. Lee, The advantage of grain refinement in the hydrogen embrittlement of Fe-18Mn-0.6C twinning-induced plasticity steel, Corros. Sci. 93 (2015) 63-69.
[47] B. Bal, M. Koyama, G. Gerstein, H.J. Maier, K. Tsuzaki, Effect of strain rate on hydrogen embrittlement susceptibility of twinning-induced plasticity steel pre-charged with high-pressure hydrogen gas, Int. J. Hydrog. Energy 41(34) (2016) 15362-15372.
[48] A. Barnoush, H. Vehoff, Electrochemical nanoindentation: A new approach to probe hydrogen/deformation interaction, Scr. Mater. 55(2) (2006) 195-198.
[49] A. Barnoush, Correlation between dislocation density and nanomechanical response during nanoindentation, Acta Mater. 60(3) (2012) 1268-1277.
[50] N. Kheradmand, R. Johnsen, J.S. Olsen, A. Barnoush, Effect of hydrogen on the hardness of different phases in super duplex stainless steel, Int. J. Hydrog. Energy 41(1) (2016) 704-712.
[51] M. Zamanzade, H. Vehoff, A. Barnoush, Effect of chromium on elastic and plastic deformation of Fe3Al intermetallics, Intermetallics 41 (2013) 28-34.
[52] A. Bamoush, N. Kheradmand, T. Hajilou, Correlation between the hydrogen chemical potential and pop-in load during in situ electrochemical nanoindentation, Scr. Mater. 108 (2015) 76-79.
[53] M. Kappes, G.S. Frankel, R. Thodla, M. Mueller, N. Sridhar, R.M. Carranza, Hydrogen Permeation and Corrosion Fatigue Crack Growth Rates of X65 Pipeline Steel Exposed to Acid Brines Containing Thiosulfate or Hydrogen Sulfide, Corrosion 68(11) (2012).
[54] I. Gutierrez-Urrutia, S. Zaefferer, D. Raabe, Electron channeling contrast imaging of twins and dislocations in twinning-induced plasticity steels under controlled diffraction conditions in a scanning electron microscope, Scr. Mater. 61(7) (2009) 737-740.
[55] R.D.K. Misra, Z. Zhang, Z. Jia, P.K.C.V. Surya, M.C. Somani, L.P. Karjalainen, Nanomechanical insights into the deformation behavior of austenitic alloys with different stacking fault energies and austenitic stability, Mater. Sci. Eng. A 528(22-23) (2011) 6958-6963.
[56] W.C. Oliver, G.M. Pharr, Measurement of hardness and elastic modulus by instrumented indentation: Advances in understanding and refinements to methodology, J. Mater. Res. 19(1) (2004) 3-20.
[57] J.L. Zhang, S. Zaefferer, D. Raabe, A study on the geometry of dislocation patterns in the surrounding of nanoindents in a TWIP steel using electron channeling contrast imaging and discrete dislocation dynamics simulations, Mater. Sci. Eng. A 636 (2015) 231-242.
[58] K. Durst, B. Backes, M. Goken, Indentation size effect in metallic materials: Correcting for the size of the plastic zone, Scr. Mater. 52(11) (2005) 1093-1097.
[59] W.S. Choi, B.C. De Cooman, S. Sandlobes, D. Raabe, Size and orientation effects in partial dislocation-mediated deformation of twinning-induced plasticity steel micro-pillars, Acta Mater. 98 (2015) 391-404.
[60] K.L. Johnson, Contact Mechanics, Cambridge University Press, Cambridge, 1987.
[61] P.M. Anderson, J.P. Hirth, J. Lothe, Theory of Dislocations, 3rd ed., Cambridge University Press, Cambridge, 2017.
[62] A. Barnoush, M. Zamanzade, Effect of substitutional solid solution on dislocation nucleation in Fe_3Al intermetallic alloys, Philos. Mag. 92(25-27) (2012) 3257-3268.
[63] C. Begau, A. Hartmaier, E.P. George, G.M. Pharr, Atomistic processes of dislocation generation and plastic deformation during nanoindentation, Acta Mater. 59(3) (2011) 934-942.

[64] A. Barnoush, H. Vehoff, Hydrogen embrittlement of aluminum in aqueous environments examined by in situ electrochemical nanoindentation, Scr. Mater. 58(9) (2008) 747-750.
[65] M. Zamanzade, H. Vehoff, A. Barnoush, Cr effect on hydrogen embrittlement of Fe3Al-based iron aluminide intermetallics: Surface or bulk effect, Acta Mater. 69 (2014) 210-223.
[66] M.Q. Chandler, M.F. Horstemeyer, M.I. Baskes, P.M. Gullett, G.J. Wagner, B. Jelinek, Hydrogen effects on nanovoid nucleation in face-centered cubic single-crystals, Acta Mater. 56(1) (2008) 95-104.
[67] P.J. Ferreira, I.M. Robertson, H.K. Birnbaum, Influence of hydrogen on the stacking-fault energy of an austenitic stainless steel, Mater. Sci. Forum 207-209 (1996) 93-96.
[68] W. Zhang, Y. Gao, Y. Xia, H. Bei, Indentation Schmid factor and incipient plasticity by nanoindentation pop-in tests in hexagonal close-packed single crystals, Acta Mater. 134 (2017) 53-65.
[69] S. Kang, Y.S. Jung, B.G. Yoo, J.I. Jang, Y.K. Lee, Orientation-dependent indentation modulus and yielding in a high Mn twinning-induced plasticity steel, Mater. Sci. Eng. A 532 (2012) 500-504.
[70] I. Karaman, H. Sehitoglu, K. Gall, Y.I. Chumlyakov, H.J. Maier, Deformation of single crystal Hadfield steel by twinning and slip, Acta Mater. 48(6) (2000) 1345-1359.
[71] S. Mahajan, G.Y. Chin, Formation of Deformation Twins in Fcc Crystals, Acta Metall. 21(10) (1973) 1353-1363.
[72] I. Gutierrez-Urrutia, S. Zaefferer, D. Raabe, The effect of grain size and grain orientation on deformation twinning in a Fe-22 wt.% Mn-0.6 wt.% C TWIP steel, Mater. Sci. Eng. A 527(15) (2010) 3552-3560.
[73] K. Durst, B. Backes, O. Franke, M. Goken, Indentation size effect in metallic materials: Modeling strength from pop-in to macroscopic hardness using geometrically necessary dislocations, Acta Mater. 54(9) (2006) 2547-2555.
[74] W.D. Nix, H.J. Gao, Indentation size effects in crystalline materials: A law for strain gradient plasticity, J. Mech. Phys. Solids 46(3) (1998) 411-425.
[75] A. Barnoush, M. Asgari, R. Johnsen, Resolving the hydrogen effect on dislocation nucleation and mobility by electrochemical nanoindentation, Scr. Mater. 66(6) (2012) 414-417.
[76] T. Zhu, J. Li, K.J. Van Vliet, S. Ogata, S. Yip, S. Suresh, Predictive modeling of nanoindentation-induced homogeneous dislocation nucleation in copper, J. Mech. Phys. Solids 52(3) (2004) 691-724.
[77] M.C. Fivel, C.F. Robertson, G.R. Canova, L. Boulanger, Three-dimensional modeling of indent-induced plastic zone at a mesoscale, Acta Mater. 46(17) (1998) 6183-6194.
[78] D. Kramer, H. Huang, M. Kriese, J. Robach, J. Nelson, A. Wright, D. Bahr, W.W. Gerberich, Yield strength predictions from the plastic zone around nanocontacts, Acta Mater. 47(1) (1998) 333-343.
[79] B.R. Lawn, A.G. Evans, D.B. Marshall, Elastic/Plastic Indentation Damage in Ceramics: The Median/Radial Crack System, J. Am. Ceram. Soc. 63(9-10) (1980) 574-581.
[80] J. Chen, S.J. Bull, On the relationship between plastic zone radius and maximum depth during nanoindentation, Surf. Coat. Technol. 201(7) (2006) 4289-4293.
[81] P.J. Burnett, D.S. Rickerby, The Mechanical Properties of Wear-Resistant Coatings I: Modeling of Hardness Behavior, Thin Solid Films 148(1) (1987) 41-50.
[82] V. Olden, C. Thaulow, R. Johnsen, Modelling of hydrogen diffusion and hydrogen induced cracking in supermartensitic and duplex stainless steels, Mater. Des. 29(10) (2008) 1934-1948.
[83] J. Crank, The Mathematics of Diffusion, 2nd ed., Oxford University Press, London, 1975.

Table 1
Chemical composition of the investigated Fe-22Mn-0.6C TWIP steel

Element	C	Mn	Al	Nb	Ti	V	N	Fe
wt. %	0.63	22.60	0.008	0.03	0.03	0.108	0.016	Bal.

Table 2
Maximum Schmid factors of different orientations under compression for preferred dislocation slip system {111}<110> and mechanical twinning system {111}<112> [69]

Deformation mode	Orientation		
	(001)	(101)	(111)
Dislocation slip	0.41	0.41	0.28
Mechanical twinning	0.47	0.25	0.16

Table 3
Sets of parameters used for modeling the L-D curves

	Values	Physical meaning
C	3	Tabor factor
M	3.06	Taylor factor
α	0.5	Empirical factor
b	0.15 nm	Burgers vector partial dislocation
ρ_{SSD}	10^{12} m^{-2}	SSD
σ_{Fric}	242 MPa	Lattice friction
θ	24.63°	Indenter factor
μ	61 GPa (101)	Shear modulus
	66 GPa (111)	
f	1.63 (air)	$\frac{\text{Plastic zone radius}}{\text{Contact area radius}}$
	1.52 (-1,250 mV)	
	1.40 (-2,000 mV)	
σ_H (101)	45 MPa (-1,250 mV)	Hydrogen contribution to lattice friction
	210 MPa (-2,000 mV)	
σ_H (111)	75 MPa (-1,250 mV)	
	340 MPa (-2,000 mV)	

Table 4
Correlation between the hardness and the hydrogen concentration at the depth of 835 nm

	Remaining hydrogen	Discharged hydrogen	Hardness recovery (001)	Hardness recovery (101)	Hardness recovery (111)
Anodic 2 h	29.2%	70.8%	68.4%	65.3%	73.8%
Anodic 20 h	3.1%	96.9%	88.3%	91.6%	90.5%

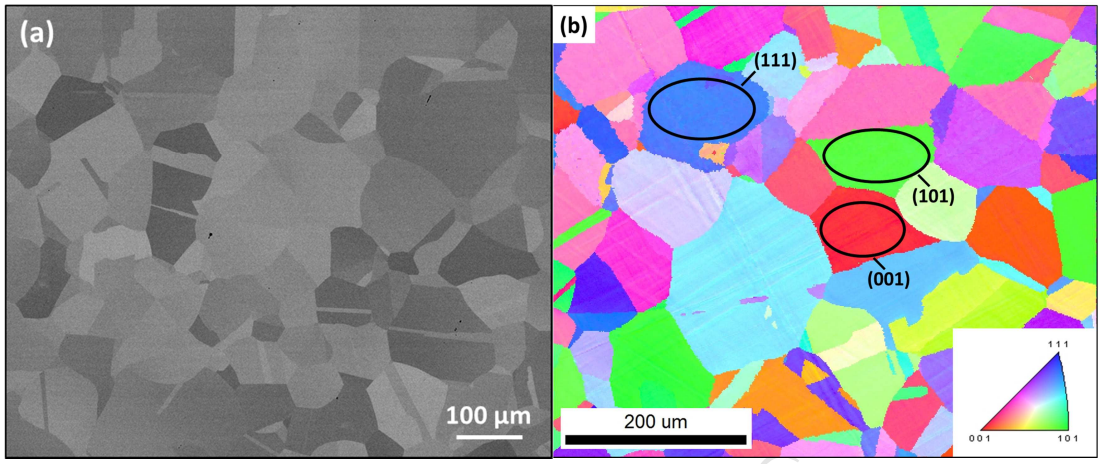

Fig. 1. (a) BSE image showing the microstructure of the investigated sample. (b) ND-IPF map of the tested sample with marked (001), (101), and (111) grains.

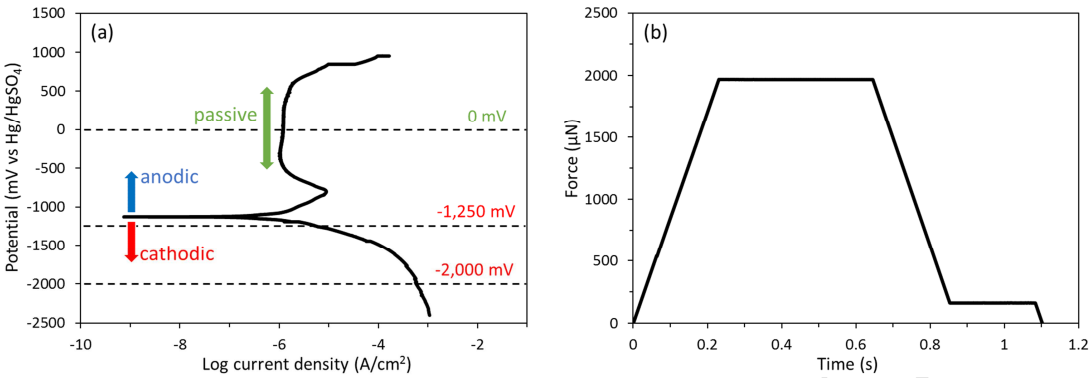

Fig. 2. (a) Polarization curve of the investigated TWIP sample. The horizontal dashed lines represent the chosen potentials for the ECNI tests. (b) Curve of the load function used for the test.

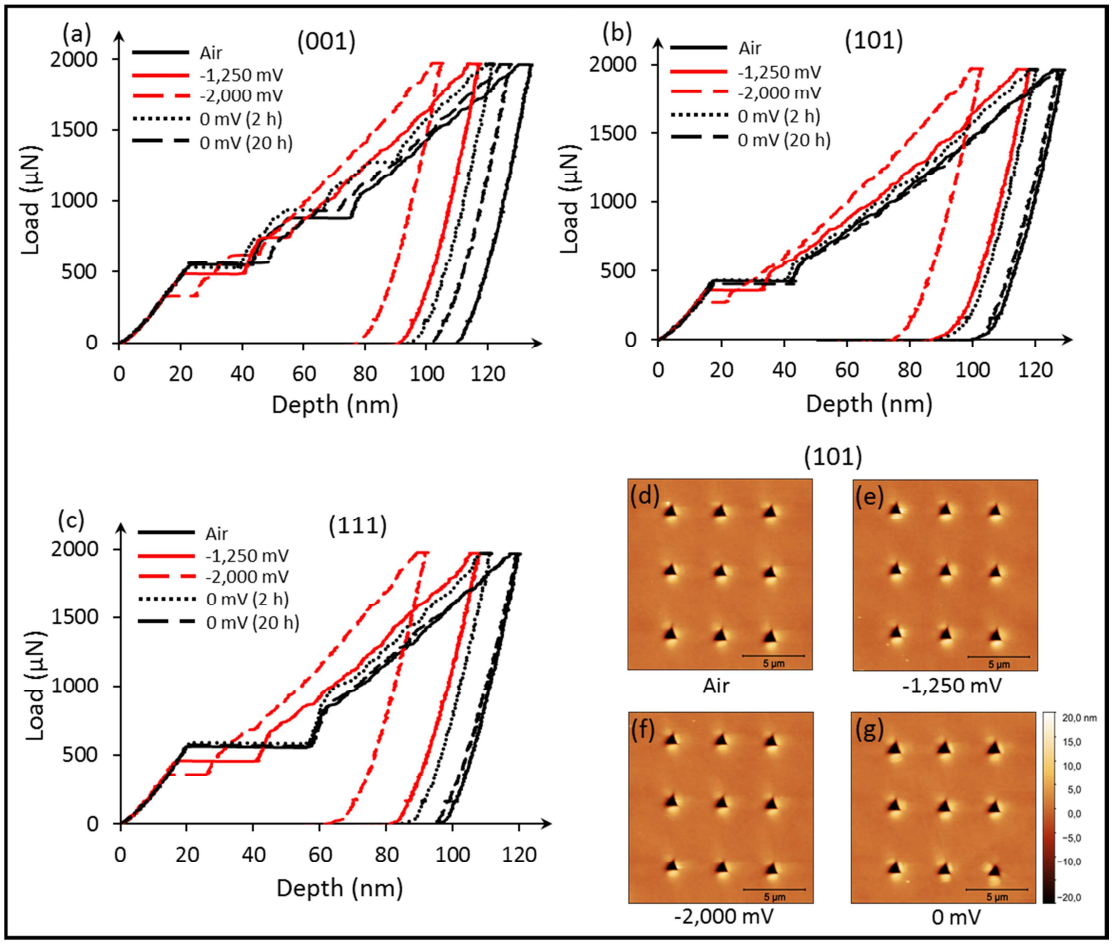

Fig. 3. Representative L-D curves for (a) (001) grain, (b) (101) grain, and (c) (111) grain tested in air, under two charging conditions and two anodic conditions. (d–g) Representative topographies after indentation in (d) air and at (e) -1,250 mV, (f) -2,000 mV, and (g) 0 mV (after 20 h) in (101) grain.

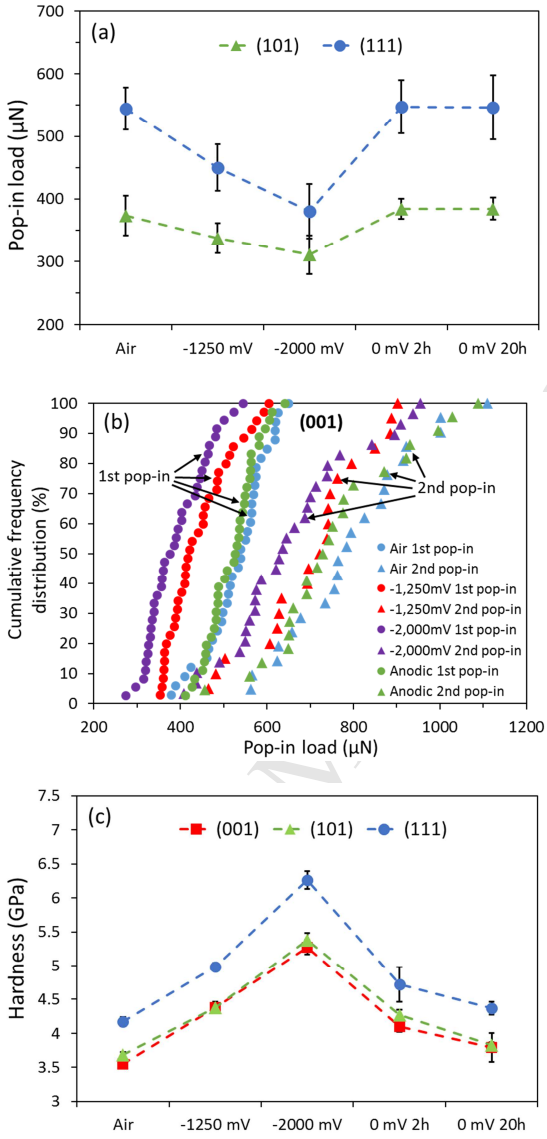

Fig. 4. Pop-in load of (a) (101) and (111) grains and (b) (001) grain; hardness values (c) under different hydrogen absorption and desorption conditions.

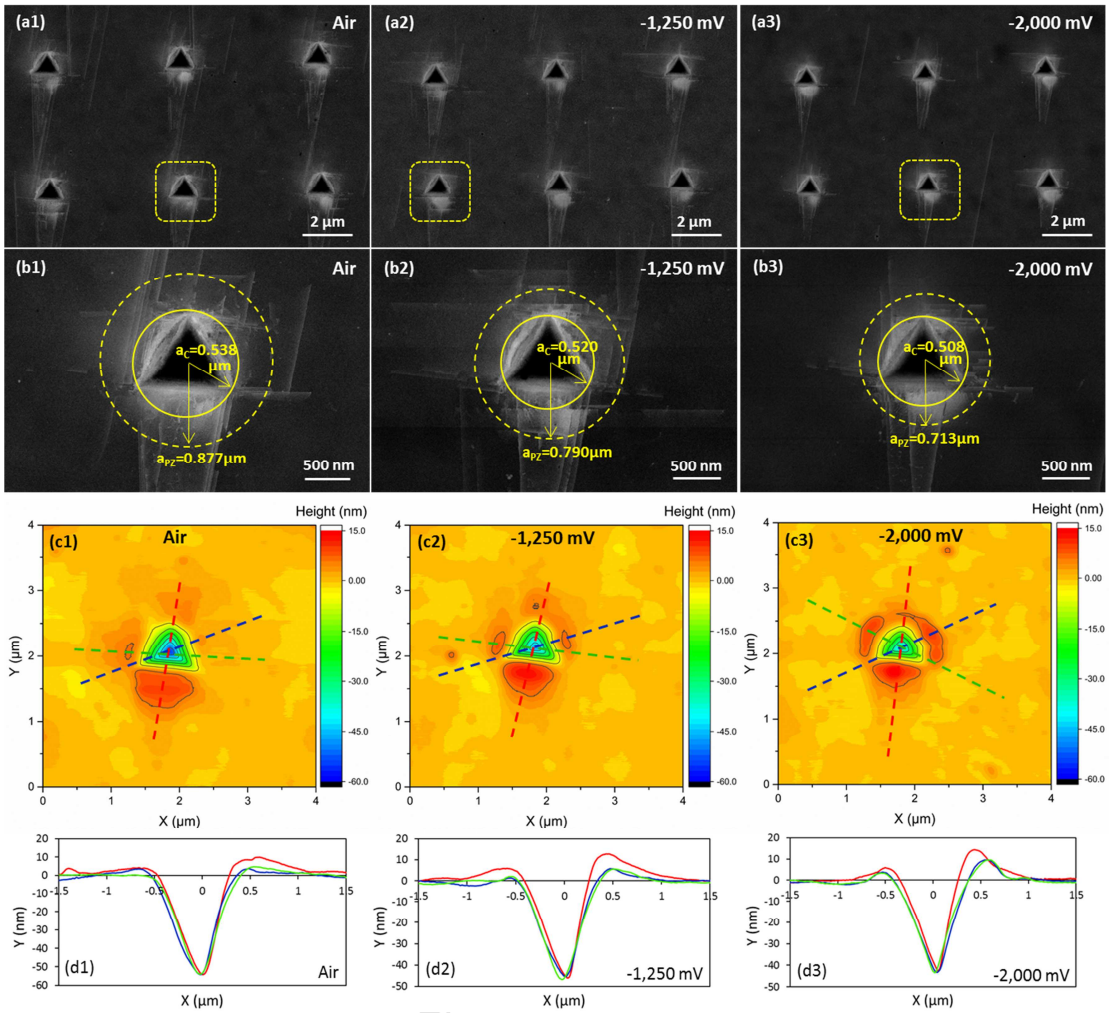

Fig. 5. Groups (a) and (b) contain ECC images of the representative indents. Group (b) contains magnified images of the indents indicating the contact area and the plastic zone. Group (c) contains the 2D color-filled contour plots showing the surface topography, and group (d) contains plots of the related pile-up data. The numbers (1), (2), and (3) represent the different testing conditions: air, -1,250 mV, and -2,000 mV, respectively. All the images are for the (101) grain.

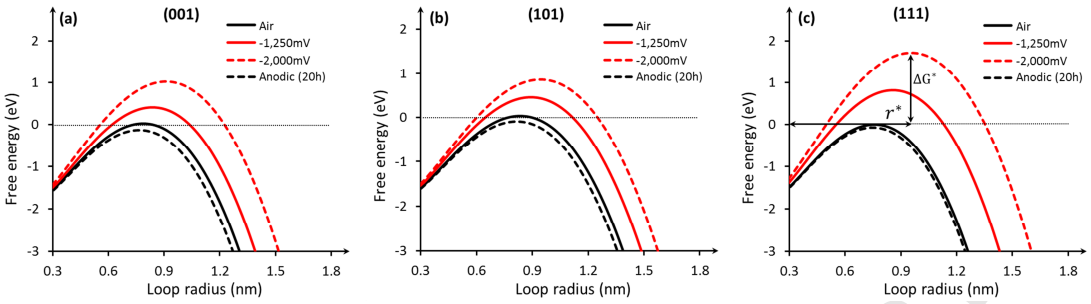

Fig. 6. Free energy of HDN with respect to the dislocation loop radius (r) for (001) (a), (101) (b), and (111) (c) grain orientations. The activation energy for HDN ($\Delta G^{\star}$) and the critical loop radius ($r^{\star}$) in the -2,000 mV charging condition are shown in (c).

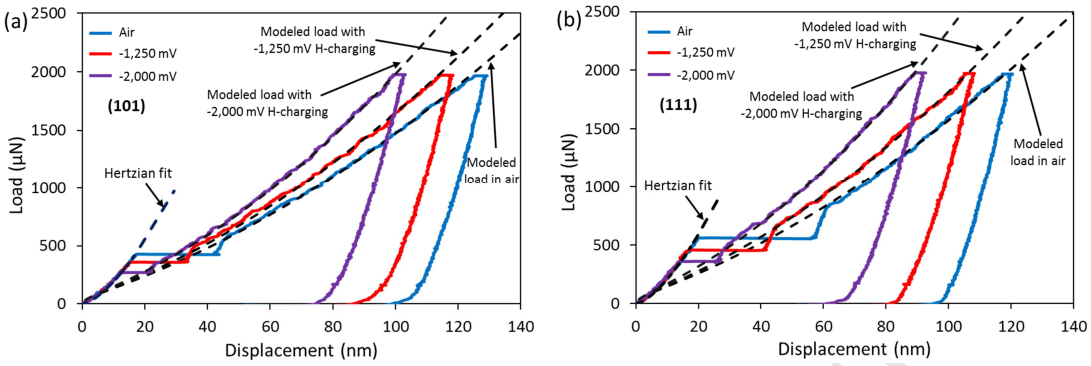

Fig. 7. Typical L-D curves of the (a) (101) grain and (b) (111) grain obtained in air and different H-charging conditions. The elastic regimes are fitted by Hertzian model. The elastoplastic parts are modeled according to Eqs. (14) and (15).

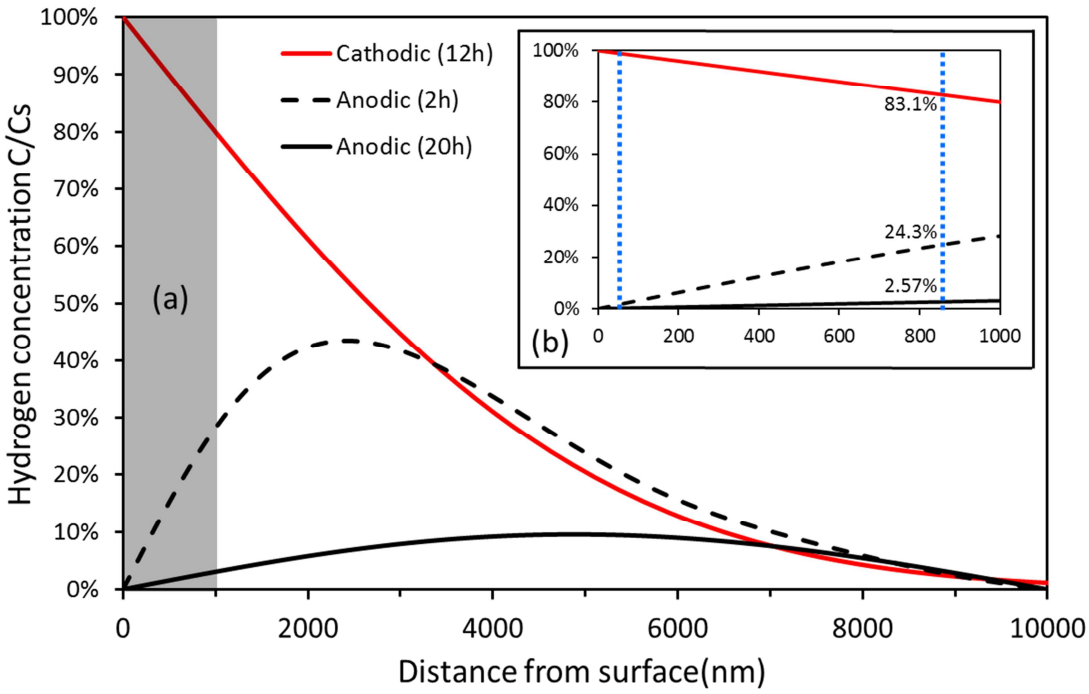

Fig. 8. (a) Hydrogen concentration profiles in different charging and aging conditions. The red line represents the hydrogen concentration after cathodic charging. The black dashed line and black solid line indicate the hydrogen concentrations after 2 h and 20 h anodic discharging, respectively. (b) Enlarged area in (a) with two blue dotted lines indicating the depths of 63 and 835 nm beneath the sample surface.